Exploring Confined Media in Hybrid Mesoporous Silicas via Thermoporosimetry

Jakub Kusz,[†,‡] Nurly Tasbolatova,[†] Cédric Boissiere,[*,¶] Clément Sanchez,[¶] and Stephane Parola[*,†]

†*École Normale Supérieure de Lyon, CNRS, Université Claude Bernard Lyon 1, Laboratoire de Chimie, UMR 5182, 46 Allée d'Italie, 69364 Lyon, France*

‡*Colloid Chemistry Department, Max Planck Institute of Colloids and Interfaces, 14476 Potsdam, Germany*

¶*Sorbonne Université, CNRS, Collège de France, Laboratoire de Chimie de la Matière Condensée de Paris (LCMCP), UMR 7574, 4 place Jussieu, 75005 Paris, France*

E-mail: cedric.boissiere@upmc.fr; stephane.parola@ens-lyon.fr

Supporting Information

1 Theoretical basis of thermoporosimety

1.1 Gibbs-Thomson equation

To derive the Gibbs-Thomson equation, one must consider a system in which solid, liquid, and gas phases exist in equilibrium. Each of the phase i is described by Gibbs-Duhem equation relating infinitesimal variations of temperature dT, pressure dP_i, and chemical potential $d\mu_i$:

$$S_i dT - V_i dP_i + n_i d\mu_i = 0, \tag{1}$$

where S_i, V_i, n_i are the entropy, volume, and number of moles of the phase i.

By taking molar volume as $\overline{V}_i = V_i/n_i$ and molar entropy as $\overline{S}_i = S_i/n_i$, we can write Gibbs-Duhem equation or solid (s), liquid (l), and gas (g) phases:

$$\overline{S}_s dT - \overline{V}_s dP_s + d\mu_s = 0, \tag{2}$$

$$\overline{S}_l dT - \overline{V}_l dP_l + d\mu_l = 0, \tag{3}$$

$$\overline{S}_g dT - \overline{V}_g dP_g + d\mu_g = 0. \tag{4}$$

On the other hand, the curvature of the interface between two phases is expressed by the Laplace equation:

$$P_j - P_i = \gamma_{ij} \frac{dA_{ij}}{dV_j}, \tag{5}$$

which for solid/liquid (sl), gas/solid (gs), and liquid/gas (lg) interfaces can be written as:

$$P_s - P_l = \gamma_{sl} \frac{dA_{sl}}{dV_s}, \tag{6}$$

$$P_g - P_s = \gamma_{gs} \frac{dA_{gs}}{dV_g}, \tag{7}$$

$$P_l - P_g = \gamma_{lg} \frac{dA_{lg}}{dV_l}. \tag{8}$$

As three phases exist in equilibrium with their interfaces at the triple point, we may also write:

$$d\mu_i = d\mu_j, \tag{9}$$

for each pair i/j.

In order to fulfill the Gibbs phase rule, we need to consider two interfaces. For melting-freezing transition in completely filled pores, we may choose solid/liquid and gas/solid interfaces (see Figure S1). In this particular case, the excess liquid at the pore exterior solidifies below normal triple point temperature T_0, and the interface remains flat at any

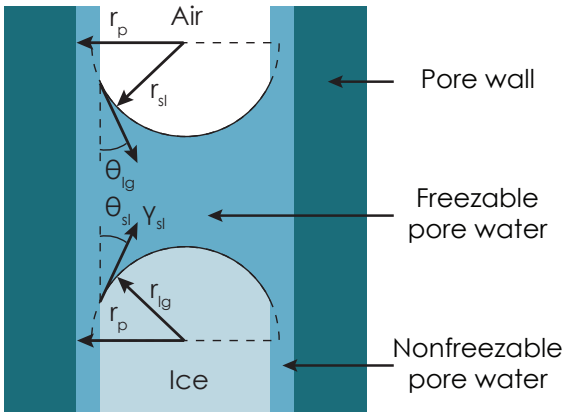

Figure S1: A scheme of confined water melting with described liquid/gas (lg) and solid/liquid (sl) interfaces.

temperature below. After the differentiation of 6 and 7 we obtain:

$$dP_s - dP_l = d\left(\gamma_{sl}\frac{dA_{sl}}{dV_l}\right), \tag{10}$$

$$dP_g - dP_s = d\left(\gamma_{gs}\frac{dA_{gs}}{dV_l}\right). \tag{11}$$

After combining these two equations, we get:

$$dP_s = dP_g - d\left(\gamma_{gs}\frac{dA_{gs}}{dV_l}\right), \tag{12}$$

$$dP_l = dP_s - d\left(\gamma_{sl}\frac{dA_{sl}}{dV_l}\right) = dP_g - d\left(\gamma_{gs}\frac{dA_{gs}}{dV_l}\right) - d\left(\gamma_{sl}\frac{dA_{sl}}{dV_l}\right). \tag{13}$$

In the next step, we subtract (3) from (2), and (4) from (2), which results in:

$$\frac{\overline{S}_s - \overline{S}_l}{\overline{V}_s - \overline{V}_l} = \frac{\overline{V}_s}{\overline{V}_s - \overline{V}_l}dP_s - \frac{\overline{V}_l}{\overline{V}_s - \overline{V}_l}dP_l, \tag{14}$$

$$\frac{\overline{S}_s - \overline{S}_g}{\overline{V}_s - \overline{V}_g} = \frac{\overline{V}_s}{\overline{V}_s - \overline{V}_g}dP_s - \frac{\overline{V}_g}{\overline{V}_s - \overline{V}_g}dP_g. \tag{15}$$

After subtracting (14) from (15) and substituting from (13) and (12) (in the experimental

conditions $dP_g = 0$) we write:

$$\left[\left(\frac{\overline{S}_g - \overline{S}_s}{\overline{V}_g - \overline{V}_s}\right) - \left(\frac{\overline{S}_l - \overline{S}_s}{\overline{V}_l - \overline{V}_s}\right)\right] dT = \frac{-\overline{V}_g}{\overline{V}_s - \overline{V}_g} d\left(\gamma_{gs}\frac{dA_{gs}}{d\overline{V}_g}\right) + \frac{\overline{V}_l}{\overline{V}_l - \overline{V}_s} d\left(\gamma_{sl}\frac{dA_{sl}}{d\overline{V}_s}\right). \quad (16)$$

As for flat interface $dA_{sg}/dV_g = 0$, the equation reduces to:

$$\left[\left(\frac{\overline{S}_g - \overline{S}_s}{\overline{V}_g - \overline{V}_s}\right) - \left(\frac{\overline{S}_l - \overline{S}_s}{\overline{V}_l - \overline{V}_s}\right)\right] dT = \frac{\overline{V}_l}{\overline{V}_l - \overline{V}_s} d\left(\gamma_{sl}\frac{dA_{sl}}{d\overline{V}_s}\right). \quad (17)$$

By assuming $\overline{V}_g \gg \overline{V}_l, \overline{V}_s$, $\overline{V}_g \gg \overline{V}_l - \overline{V}_s$ and substituting $\overline{S}_s - \overline{S}_l = \Delta\overline{S}_f$, one arrives to:

$$-\Delta\overline{S}_f dT = \overline{V}_l \gamma_{sl} d\left(\frac{dA_{sl}}{dV_s}\right). \quad (18)$$

We can substituted $T\Delta\overline{S}_f = \Delta\overline{H}_f$:

$$-\Delta\overline{H}_f \frac{dT}{T} = \overline{V}_l \gamma_{sl} d\left(\frac{dA_{sl}}{dV_s}\right). \quad (19)$$

After integrating from T_0 to T for the transition from a flat ($dA_{sl}/dV_s = 0$) to curved interface (dA_{sl}/dV_s) we obtain:

$$ln\frac{T}{T_0} = -\frac{\overline{V}_l \gamma_{sl}}{\Delta\overline{H}_f}\frac{dA_{sl}}{dV_s}. \quad (20)$$

We can also approximate

$$ln\frac{T}{T_0} = ln\frac{T_0 - \Delta T}{T_0} = ln\left(1 - \frac{\Delta T}{T_0}\right) \cong -\frac{\Delta T}{T_0}, \quad (21)$$

and substitute molar volume as $\overline{V}_l = M/\rho_l$, and molar enthalpy of fusion as $\Delta\overline{H}_f = \Delta h_f M$, where M is the molar weight of liquid, ρ_l is its density, and Δh_f is the specific enthalpy of fusion. That allows us to obtain the general form of the Gibbs-Thomson equation:

$$\Delta T = \frac{T_0 \gamma_{sl}}{\Delta h_f \rho_l}\frac{dA_{sl}}{dV_s}. \quad (22)$$

It can be further adapted for spherical

$$\Delta T = \frac{T_0 \gamma_{sl}}{\Delta h_f \rho_l} \frac{2}{r} = \frac{T_0 \gamma_{sl}}{\Delta h_f \rho_l} \frac{2cos\theta}{r_p}, \tag{23}$$

or cylindrical pores

$$\Delta T = \frac{T_0 \gamma_{sl}}{\Delta h_f \rho_l} \frac{1}{r} = \frac{T_0 \gamma_{sl}}{\Delta h_f \rho_l} \frac{cos\theta}{r_p}. \tag{24}$$

The relation between the radius of the pore and the interface is given as $r_p = rcos\theta$, where θ is the contact angle.

1.2 Pore size distribution

The initial heat-flow curve dQ/dt can be translated into the pore size distribution by following the formula:

$$\frac{dV_p}{dr_p} = \frac{dQ}{dt} \frac{dt}{d(\Delta T)} \frac{d(\Delta T)}{dr_p} \frac{1}{m \Delta h_f(T) \rho(T)}, \tag{25}$$

where $d(\Delta T)/dt$ is the heating rate, ρ, and Δh_f are the temperature-dependent density and transition enthalpy of the confined liquid. $\frac{d(\Delta T)}{dr_p}$ is calculated as a derivative of the Gibbs-Thomson equation or the empirical equation describing the melting point depression as a function of pore radius. The main difficulty in using this equation comes from the lack of exact data about the values of $\rho(T)$ and $\Delta h_f(T)$. While empirical relations for water can be found in the literature, usually, there is insufficient data about temperature dependencies for density and fusion enthalpy for organic solvent.[1] In such a case, constant values must be assumed.

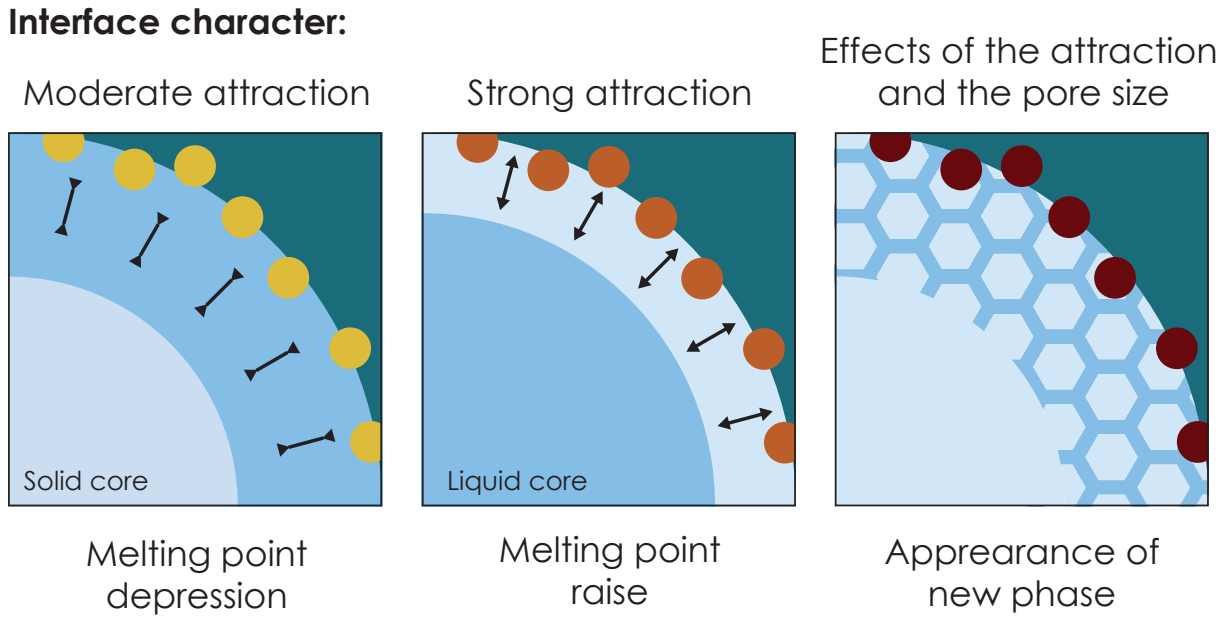

Figure S2: Schematic representation of possible types of interaction between the hybrid material and confined solvent. Dots of different color represent organic functions of different chemical characteristics. Weak and modern attraction leads to melting point depression, while strong interaction increases the transition temperature. The appearance of new phases is driven by a combination of effects of pore geometry and the attraction at the interface.

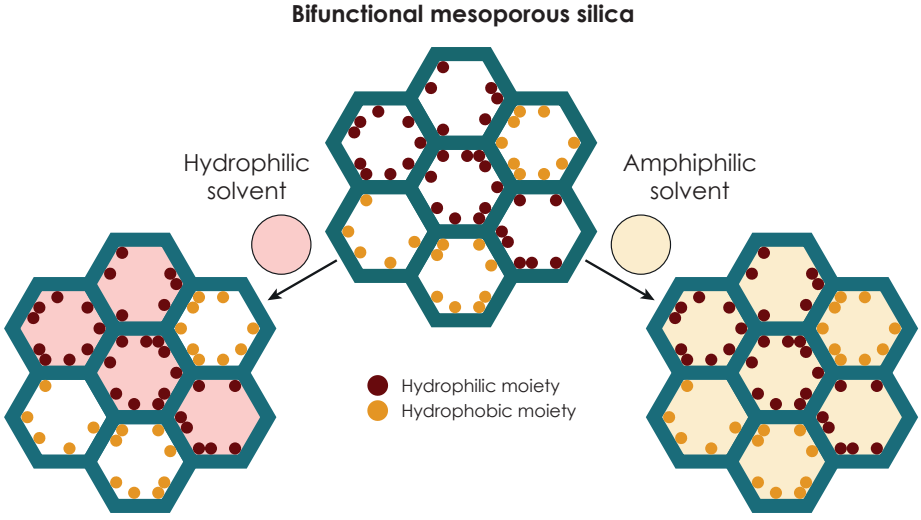

Figure S3: Concept of adapting TPM to characterization of species distribution in bifunctional hybrid materials. If two different functions segregate between pores, molecular "patches" may appear. By using solvents with different affinity to these groups (hydrophobic, hydrophilic, amphiphilic), we should be able to fill the pores selectively and characterize them with thermoporosimetry.

2 Optimization of synthesis of mesoporos particles

2.1 Water content in sols

When particles are synthesized from a sol with too low water-to-silica molar ratio ($n_{\mathrm{water}}/n_{\mathrm{Si}} = 20$), the resulting porosity is unsatisfactory (Figure S4). This is likely due to the significantly higher evaporation rate during spray drying compared to dip-coating, for which this water content is typically used. To slow the evaporation and support better pore formation, we increased the water content to $n_{\mathrm{water}}/n_{\mathrm{Si}} = 40$. Additionally, a more aqueous environment favors the micellization of the copolymer templates due to the presence of hydrophobic segments in their structure.

Figure S4 compares DSC thermograms of water confined in samples synthesized at both water concentrations (P1-W40 vs. P1-W20 and F0.5-W40 vs. F0.5-W20). In both cases, the endothermic peak observed for the higher water content sample is more intense and well-defined, suggesting improved pore formation and a narrower pore size distribution.

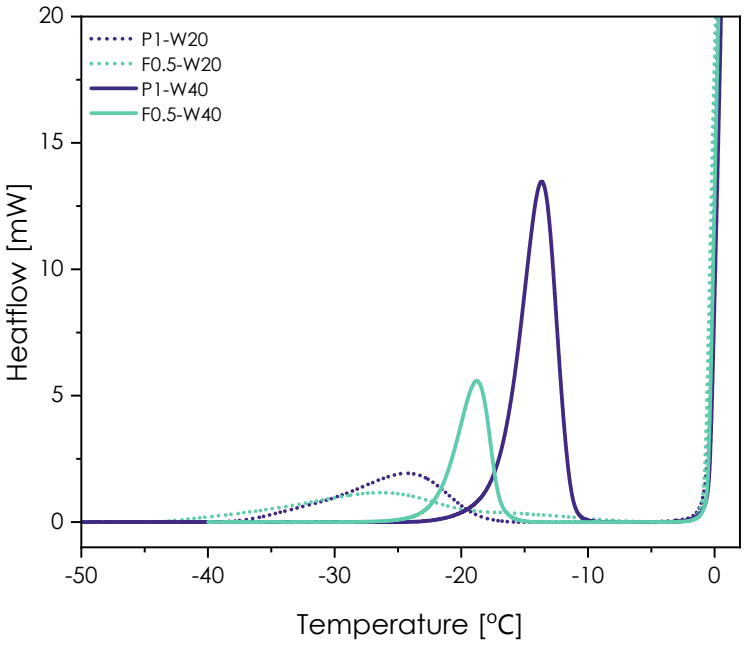

Figure S4: Thermograms obtained for pluronic-templated particles prepared with molar ratios of H_2O to Si equal 20 and 40 (samples denoted as W20 and W40, respectively). Peaks of water confined in pores of P1-W40 and F0.05-W40 have better resolution and intensity.

2.2 Spray-drying temperature

The spray-drying temperature did not significantly affect the mesopore size in non-hybrid silica particles. Figure S5 shows that samples prepared with F127 and dried at 180, 200, and 220°C exhibit similar melting point depressions in the confined water, indicating comparable pore structures.

However, maintaining the appropriate drying temperature is critical. Excessively high temperatures can cause abrupt drying, hindering mesostructure formation, while too low temperatures can prevent complete condensation of silica or cause the copolymer to melt prematurely, resulting in poor powder formation. Therefore, we selected 200°C at the inlet and 100°C at the outlet as optimal spray-drying temperatures.

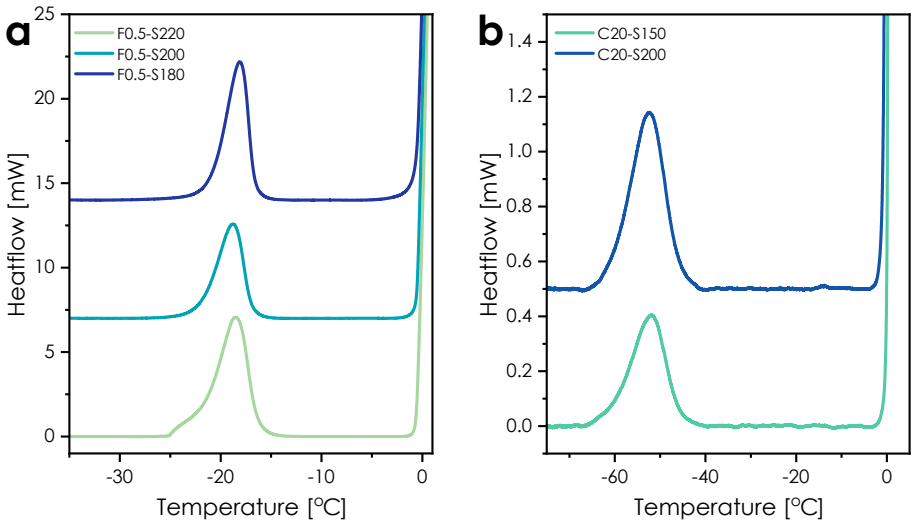

Figure S5: **Influence of the spray drying temperature on the porosity of the material. a,** Endothermic peaks of water are present at the same temperature for F127-templated particles prepared at 180, 200, and 220°C, suggesting the same pore size. **b,** Endothermic peaks of water confined in mesopores of CTAB-templated silica sprayed at 150 and 200°C.

2.3 Template removal

To preserve the integrity of organic functional groups in hybrid materials, non-ionic template removal must be performed under mild conditions. Several methods were tested to optimize this step. Before template removal, all particles were thermally stabilized at 80°C for three days to strengthen the silica network. Higher stabilization temperatures (e.g., 130°C) risk early template decomposition, potentially damaging the mesostructure.

For comparison, the P1-400 sample was calcined at 400°C (2°C/min ramp, 5-hour plateau). Other samples (P1-A6 and P1-E6) were subjected to 6-hour Soxhlet extraction using either acetone or acidified ethanol (EtOH 94.6 wt% + HCl 0.5 wt%).[2] An extended 12-hour ethanol extraction was applied to the P1-E12 sample. These were compared with the raw P1-R sample and a thermally treated but unextracted sample, P1-130.

FTIR spectroscopy and thermogravimetric analysis (TGA) were used to evaluate the template removal efficiency. In the IR spectrum of P1-R (Figure S6a), characteristic vibrational bands of Pluronic P123 are observed:ν(C−H) stretching at 2971 and 2880 cm^{-1}, symmetric

deformation and wagging modes at 1374 and 1343 cm^{-1}, and twisting modes at 1288 and 1242 cm^{-1}.[3,4] The ν(C−O−C) band is masked by the broad ν(Si−O−Si) band at 1103 cm^{-1}. A reduction in these signals reflects template removal efficiency. Complete removal is seen only in the calcined P1-400 sample, while extracted samples show significant but incomplete template reduction. Notably, a peak at 1730 cm^{-1}, corresponding to carbonyl (C=O) groups, emerges in extracted samples—likely due to partial oxidation of P123. All samples also show δ(H−O−H) bending at 1630 cm^{-1} related to physisorbed water.

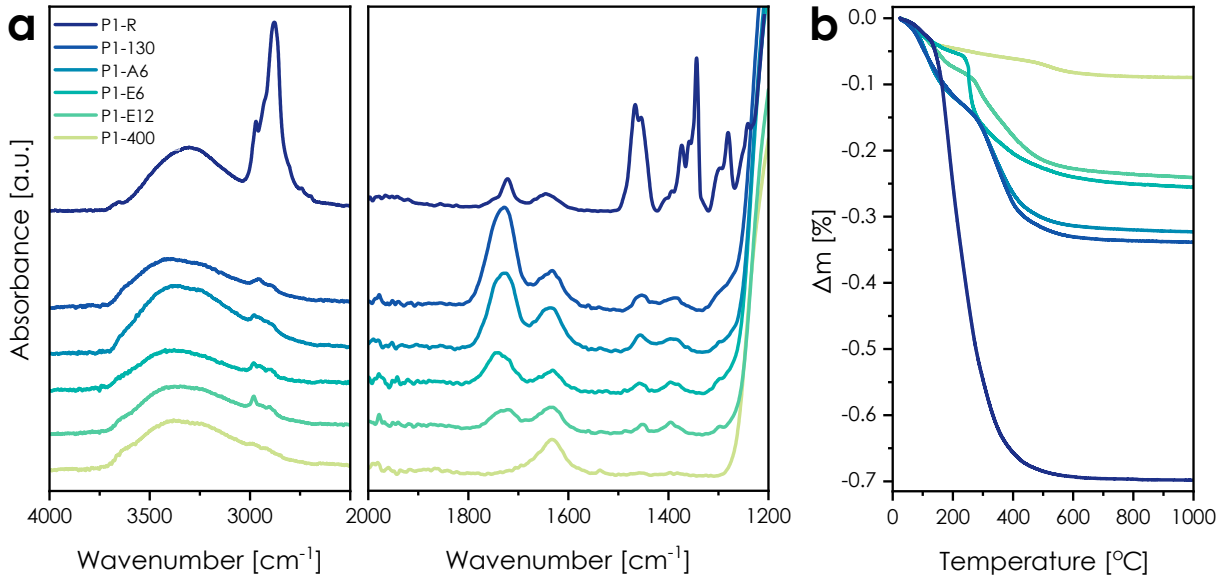

Figure S6: Analysis of the template elimination method. a, (from the top) Infrared spectra of raw, stabilized, extracted with, and calcined samples. The latter method results in complete template removal. b, Thermogravimetric analysis results. The Δm occurring above 200°C corresponds to the decomposition of pluronic F127. The smallest mass loss is observed for the P1-400 sample.

The mass losses in the ranges 0-150 and 150-300°C seen during thermogravimetric analysis (Figure S6b). correspond to the desorption of water and decomposition of the pluronic P123, respectively. One has to notice that a part of the mass loss is due to the loss of water molecules during TGA from silanol condensation. It is superimposed to other mass losses up to 600°C. It is common to loosen by this way about 10 wt% of a dry sol-gel silica before 500°C.

The latter, corresponding to SDA decomposition, is most significant for the raw P1-R sample, while the P1-400 powder exhibits only a very slight mass drop around 500°C. The extracted samples are found between these two extremes, which is in agreement with FTIR results. The extraction was the most effective for P1-E12, but complete template removal can be achieved only by calcination at 400°C. A significant decomposition of pluronic occurs during the treatment at 130°C, as we can see from the smaller mass loss in TGA and the decrease in the intensity of the P123 bands in the IR spectrum.

2.4 DSC heating rate

To allow continuous thermal equilibrium, samples should be heated as slowly as possible. However, the phase transition is a dynamic process, and the sample is never in a "true" equilibrium state during the measurement.[5] On the other hand, a small heating rate results in a high noise-to-signal ratio, which may make the data analysis more ambiguous.[6] To validate the heating rate's influence on the obtained signal, we performed several DSC scans on a P1 sample using water as a confinement agent. The crucible was cooled down to -100°C and heated to RT with a speed of 5, 10, and 20 °C/min. As we can see in Figure S7, the highest rate results in the strongest signal, as the value of delivered heat per time unit must be the highest. However, there is a small shift of the peak maximum compared with the sample heated at 5 °C/min. It suggests a delay between the input signal and the measured responses, known as the thermal lag. Rapid heating prevents the system from reaching a uniform temperature and thermodynamic equilibrium instantaneously, which is particularly important regarding the accuracy and reproducibility of the TPM analysis. To reach a compromise between these two factors, we decided to use 5 °C/min as a standard heating rate when using water or decane as probe liquids and 20 °C/min for benzene and 1,2,4-trichlorobenzene. In these conditions, samples give measurable responses while being sufficiently close to the equilibrium state. Importantly, we observed no difference in thermal response if the same sample was heated over several cycles at the same rate. This shows that repeated freezing

and melting of water inside the pores does not affect the mesostructure.

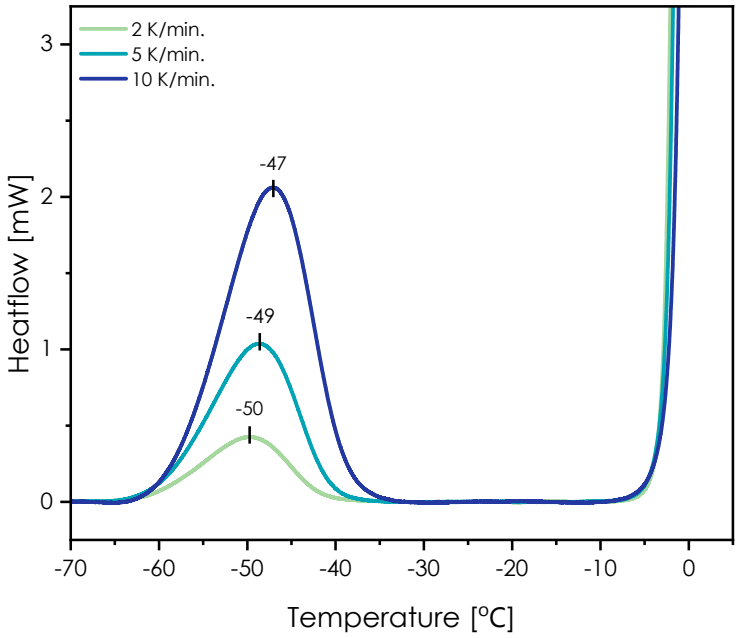

Figure S7: Thermograms obtained with different heating rates for P1-400 powder. The endothermic peak of confined water increases the intensity and shifts toward higher temperatures with the heating rate.

3 Supplementary data

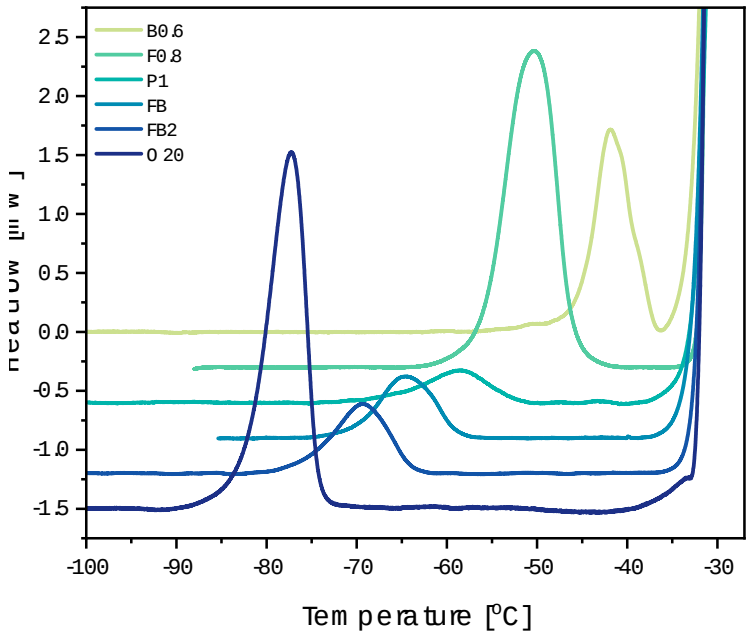

Figure S8: DSC thermograms obtained for decane solid-liquid transition in pores of non-hybrid silicas used for calibration.

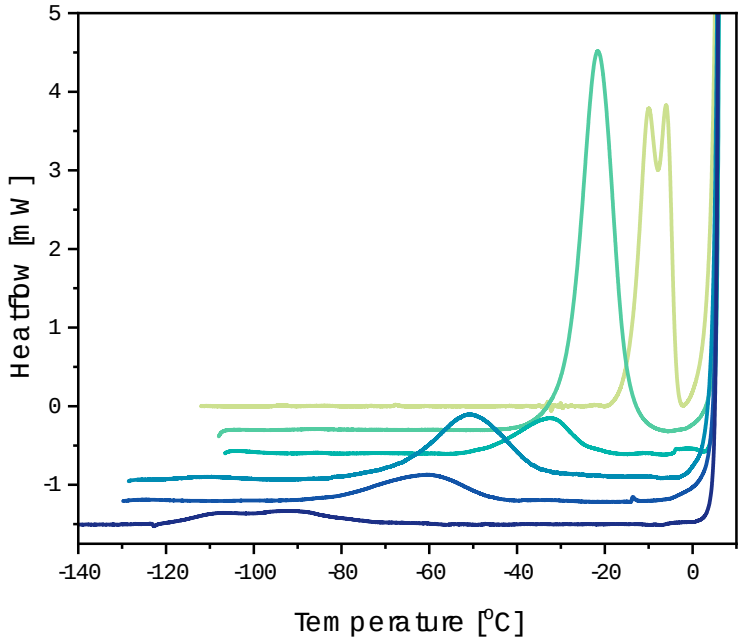

Figure S9: DSC thermograms obtained for benzene solid-liquid transition in pores of non-hybrid silicas used for calibration.

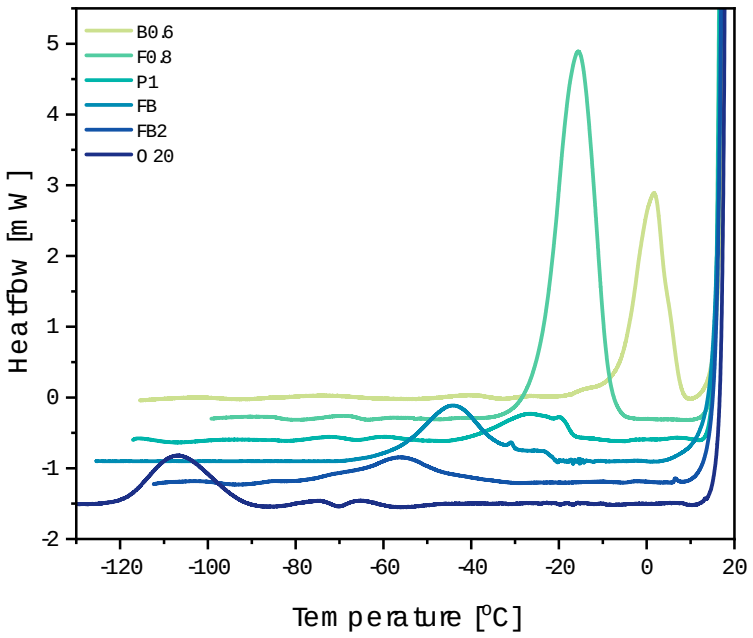

Figure S10: DSC thermograms obtained for TCB solid-liquid transition in pores of non-hybrid silicas used for calibration.

Table 1: TPM calibration equation describing the relation between the pore radius r and the melting point depression ΔT for water, decane, benzene, and TCB.

Solvent	TPM equation	Source
Water	$r = \frac{33.3}{\Delta T} + 0.8$	Ishikiriyama *et al.*[7]
	$r = \frac{19.082}{\Delta T + 0.1207} + 1.12$	Landry[1]
Decane	$r = 0.94 exp(\frac{1}{0.033 \Delta T})$	Bahlou *et al.*[8]
Benzene	$r = \frac{131.6}{\Delta T} + 0.54$	Brun *et al.*[9]
TCB	$r = 1.47 exp(\frac{1}{0.0308 \Delta T})$	Billamboz *et al.*[10]

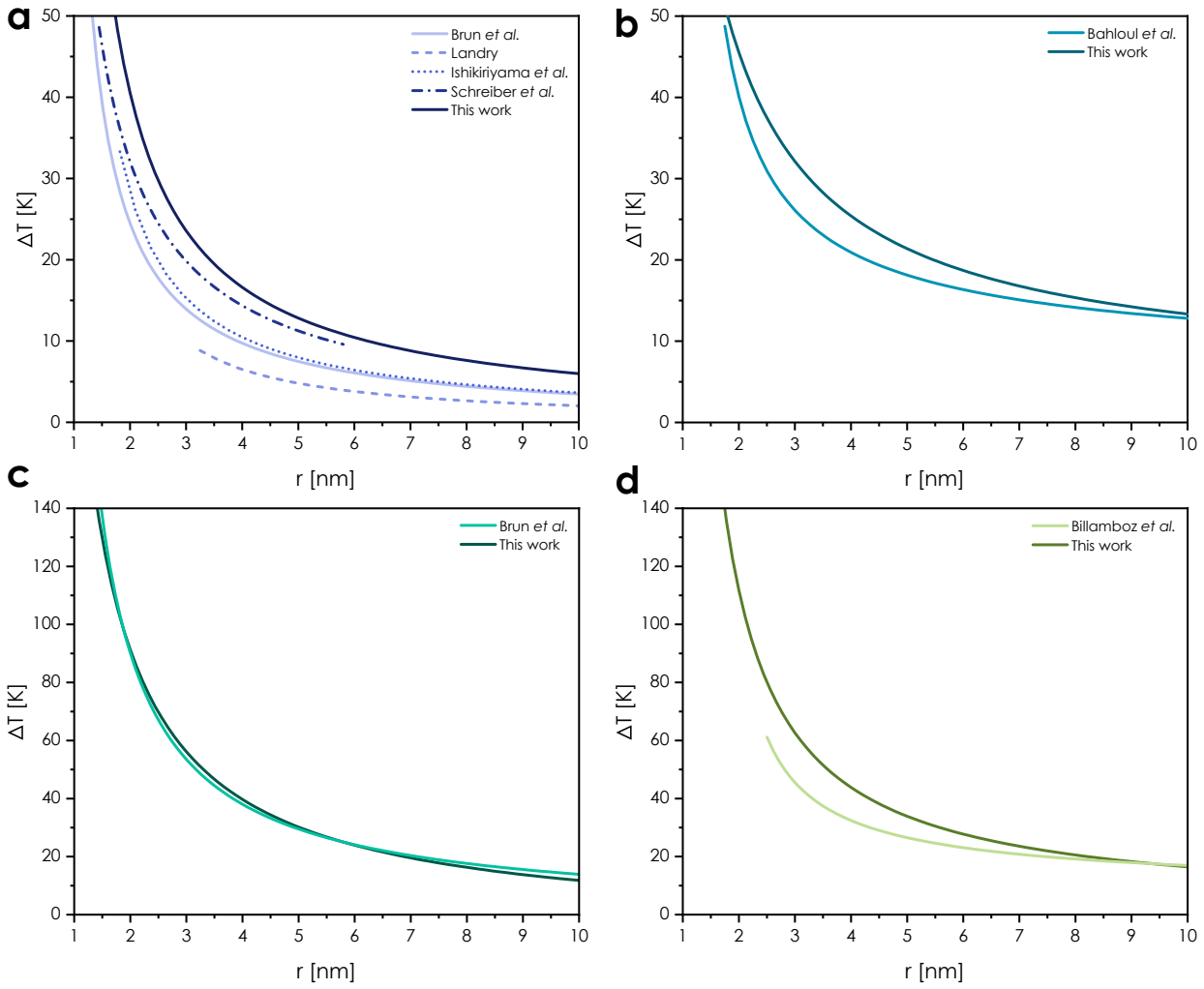

Figure S11: Comparision between our ΔT-r calibration curves and those obtained by other authors (see Table 1) for (a) water; (b) decane; (c) benzene; and (d) TCB.

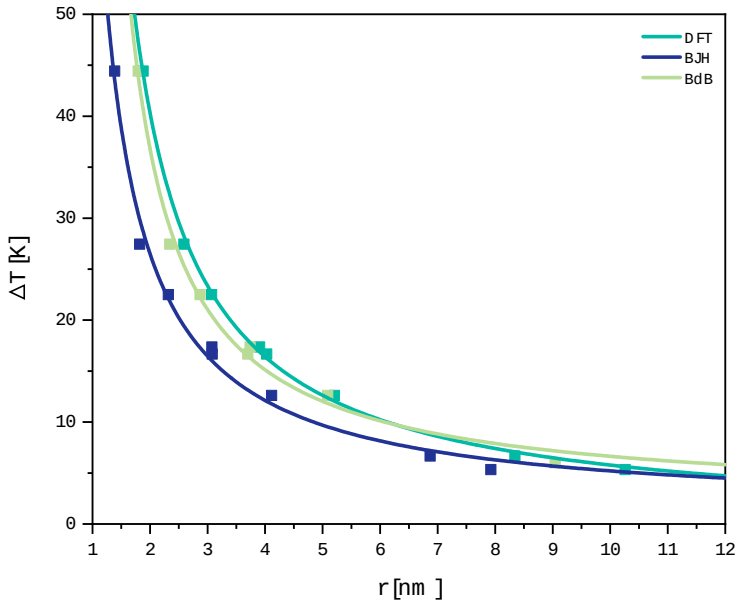

Figure S12: Comparison between ΔT-r calibration curves derived from the same TPM data (with water as probe liquid) but different methods of interpreting the N2 sorption isotherms. BJH and Broekhoff-de Boer PSD were based on the adsorption branches of the isotherms. For Broekhoff-de Boer analysis, we used the method described by Prouzet et al.[11]

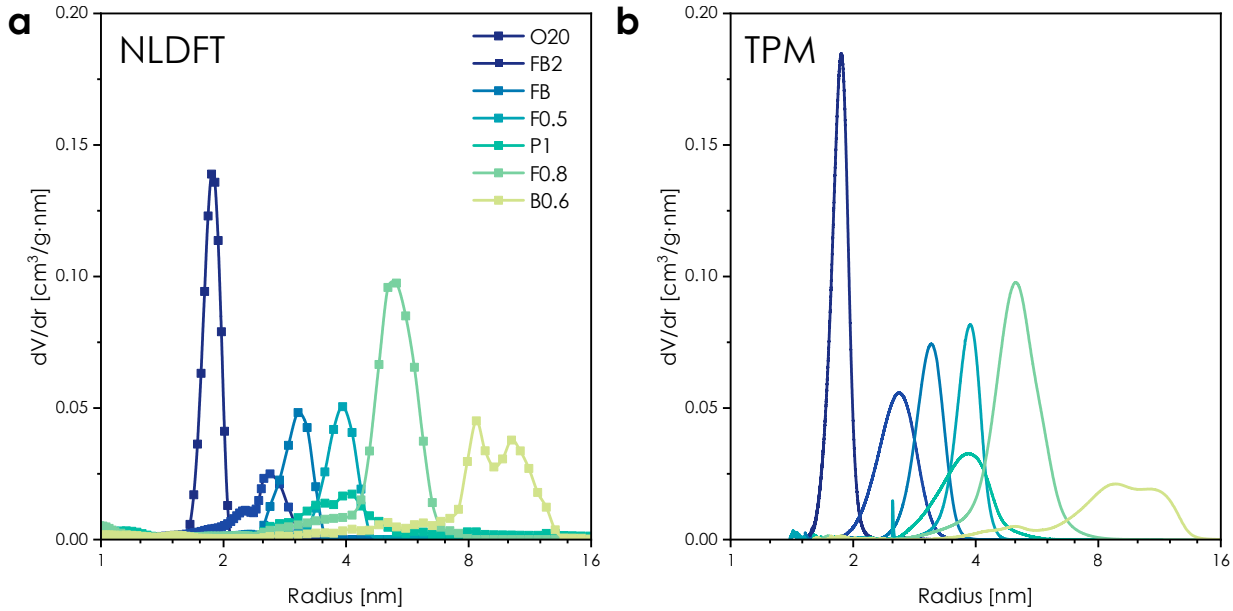

Figure S13: Pore size distributions calculated from (a) gas sorption and (b) the thermoporosimetry .

Table 2: Comparison of widths (FWHM/mean) of PSD calculated from gas sorption (NLDFT) and the thermoporosimetry.

	NLDFT			TPM		
Sample	r [nm]	FWHM [nm]	FWHM/r [%]	r [nm]	FWHM [nm]	FWHM/r [%]
B0.6	9.65	3.77	39.1	9.79	5.32	54.3
F0.8	5.37	1.4	26.1	5.11	1.39	27.1
F0.5	3.93	0.76	19.3	3.85	0.60	15.5
P1	3.81	1.6	42.0	3.80	1.22	32.2
FB	3.05	0.56	18.4	3.11	0.55	17.8
FB2	2.62	0.55	21.0	2.59	0.63	24.4
O20	1.88	0.22	11.7	1.86	0.20	10.6

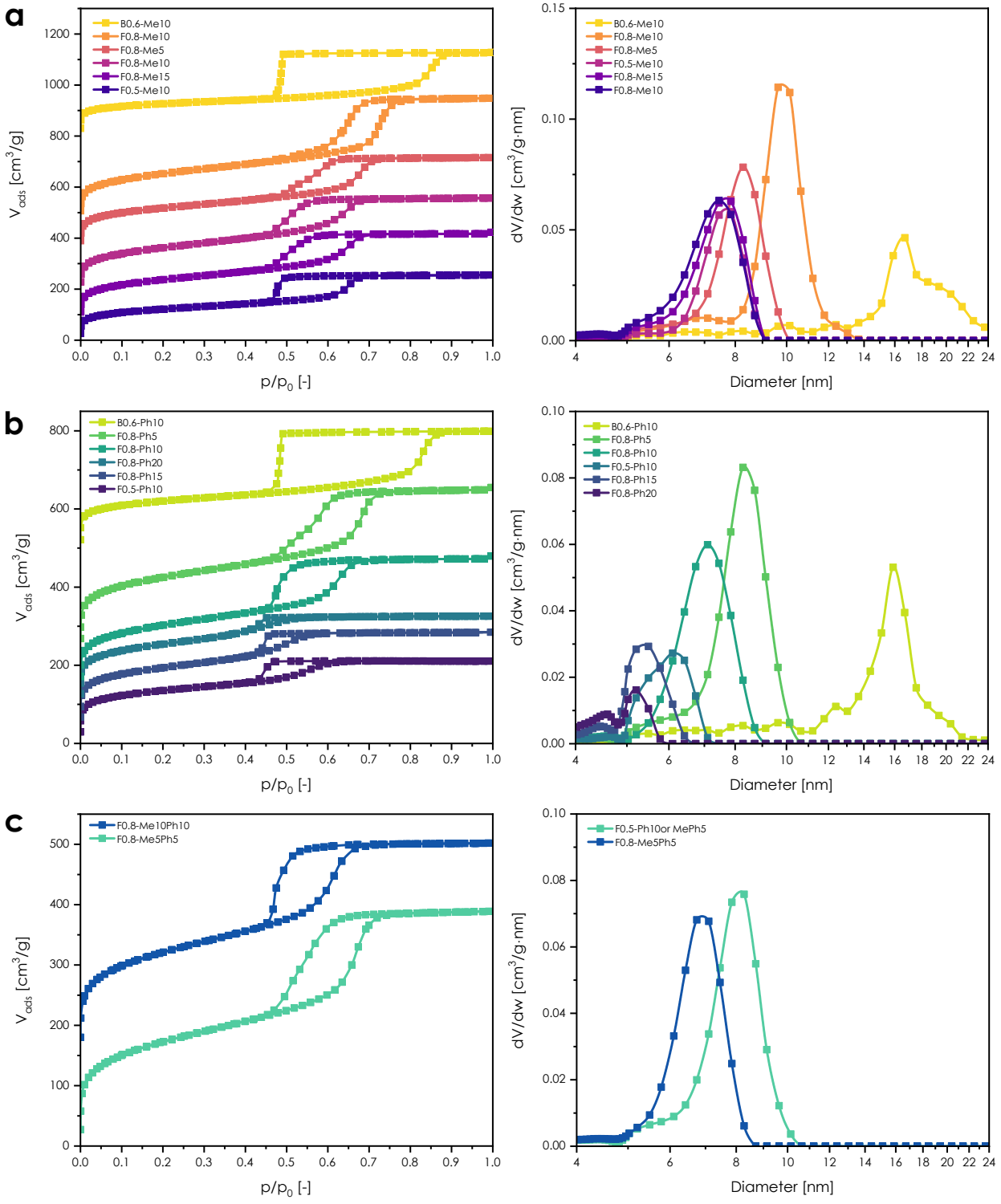

Figure S14: N_2 adsorption-desorption isotherms and corresponding PSDs for mesoporous silicas functionalized with (a) methyl; (b) phenyl; (c) methyl and phenyl groups.

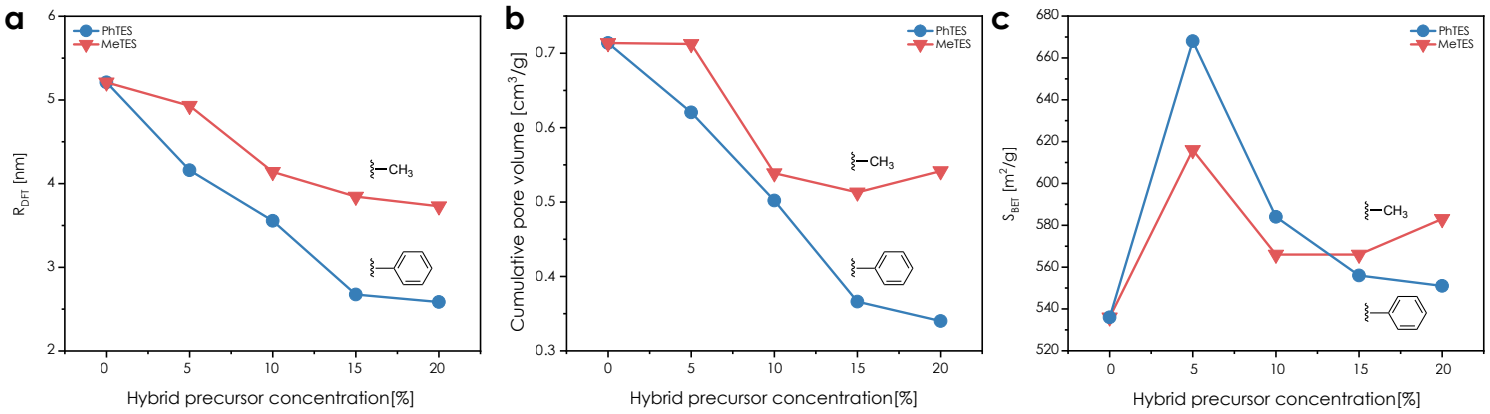

Figure S15: Evolution of the structural properties of hybrid silicas as a function of precursor concentration. (a) Mean pore radius;(b) Cumulative pore volume; (c) Specific surface area. Red and blue points correspond to materials functionalized with methyl and phenyl, respectively.

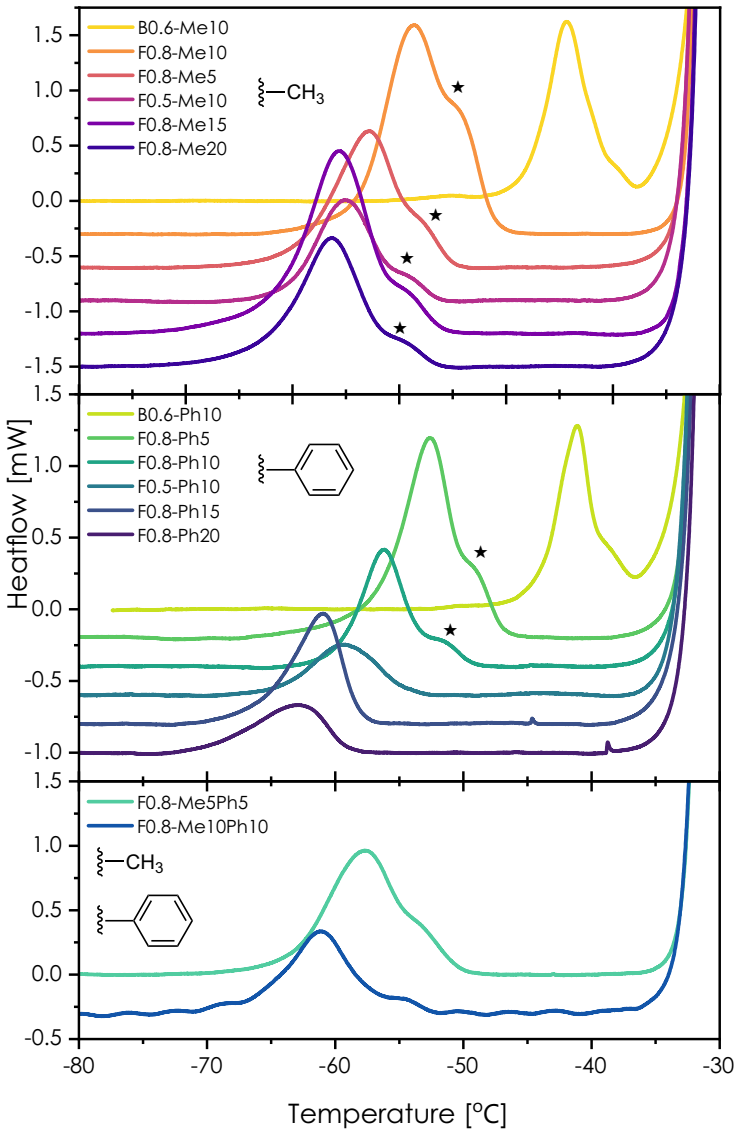

Figure S16: DSC thermograms obtained for decane solid-liquid transition in pores of hybrid silicas functionalized by one-pot method with methyl (top), phenyl (middle), and methyl and phenyl (bottom) groups.

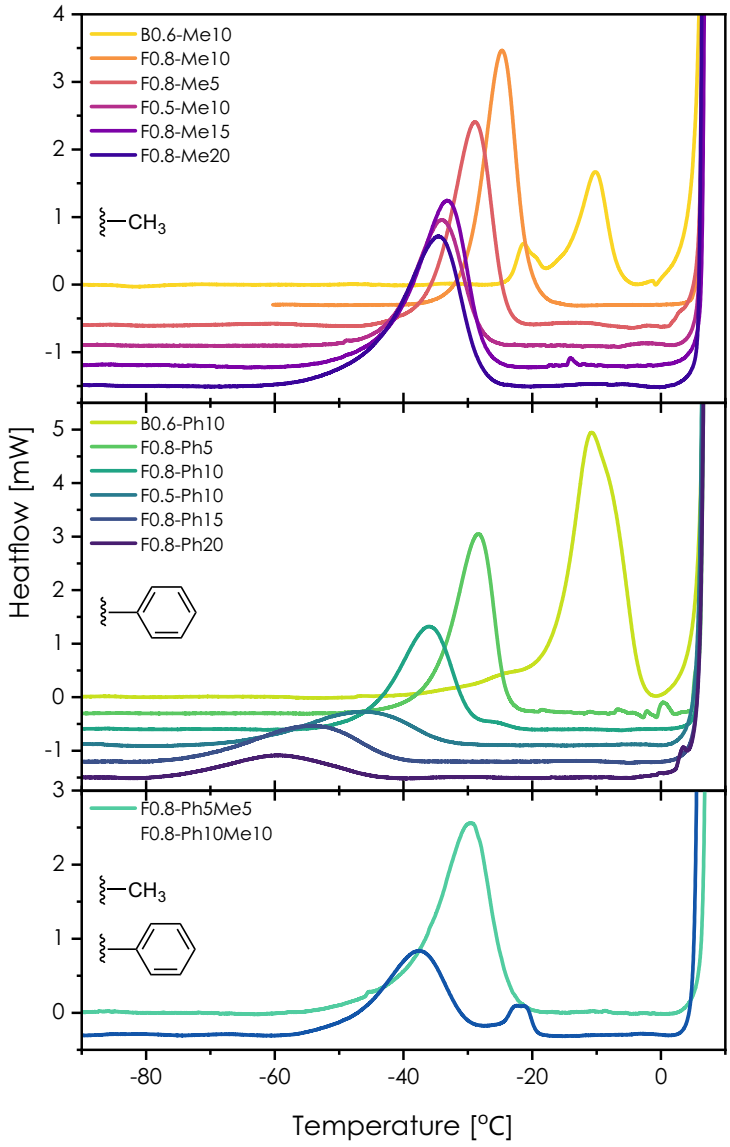

Figure S17: DSC thermograms obtained for benzene solid-liquid transition in pores of hybrid silicas functionalized by one-pot method with methyl (top), phenyl (middle), and methyl and phenyl (bottom) groups.

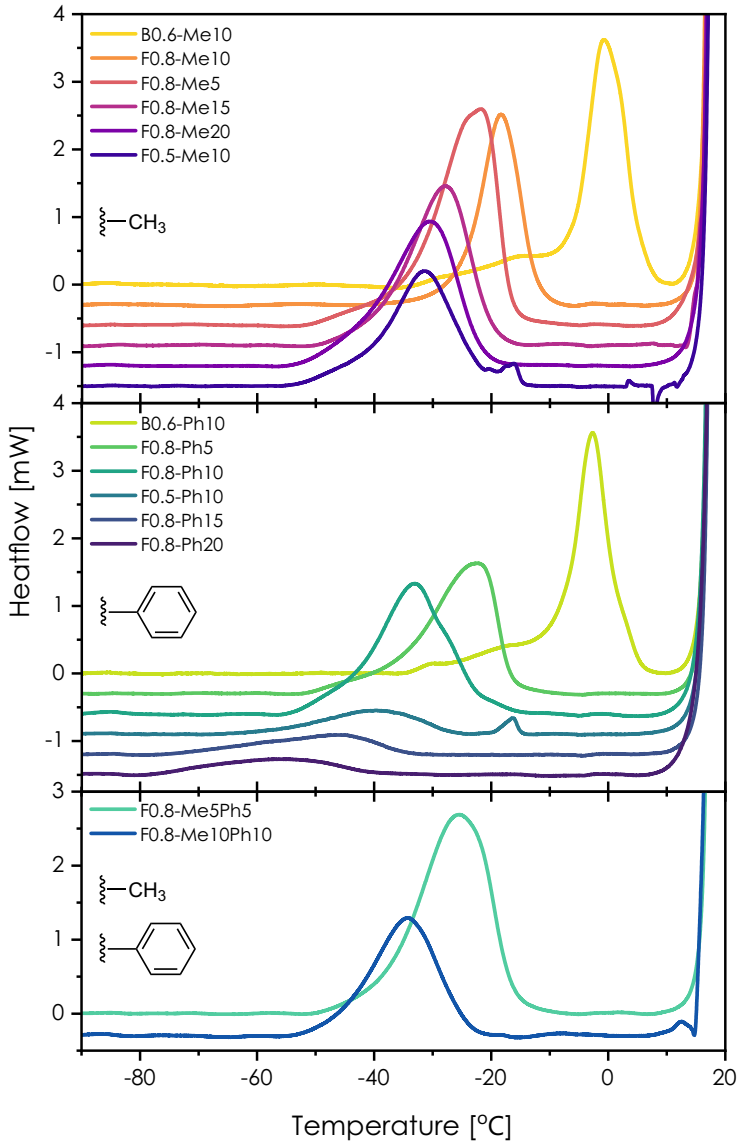

Figure S18: DSC thermograms obtained for TCB solid-liquid transition in pores of hybrid silicas functionalized by one-pot method with methyl (top), phenyl (middle), and methyl and phenyl (bottom) groups.

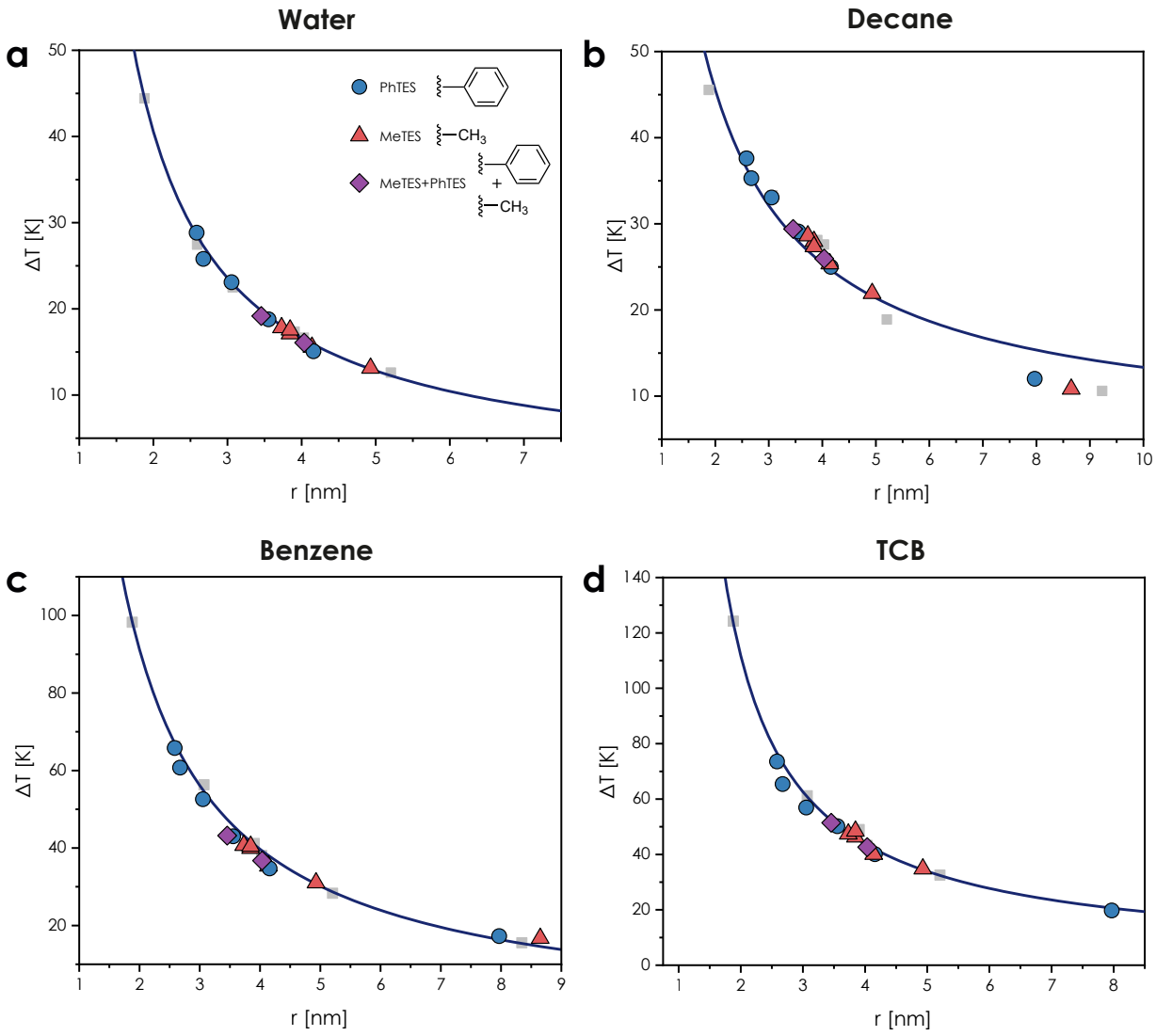

Figure S19: Experimental values of melting point depression, ΔT, observed for (a) water; (b) decane; (c) benzene; and (d) TCB confined in hybrid materials functionalized with MeTES ($\triangle$), PhTES ($\triangledown$), and both MeTES and PhTES ($\diamond$).

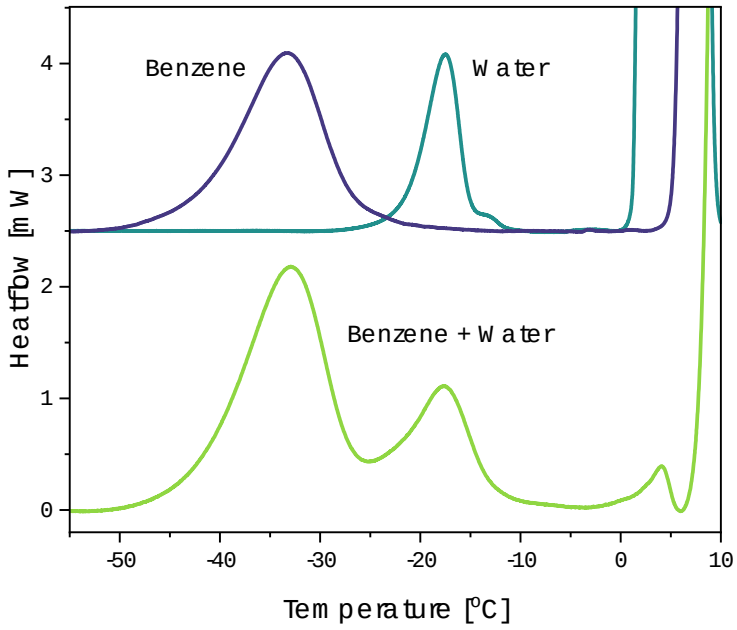

Figure S20: DSC thermograms obtained for a mixture of water and benzene confined in the pores of hybrid F0.8-Ph10 silica. On the top thermograms of pure water and pure benzene confined in the same material are presented for comparison.

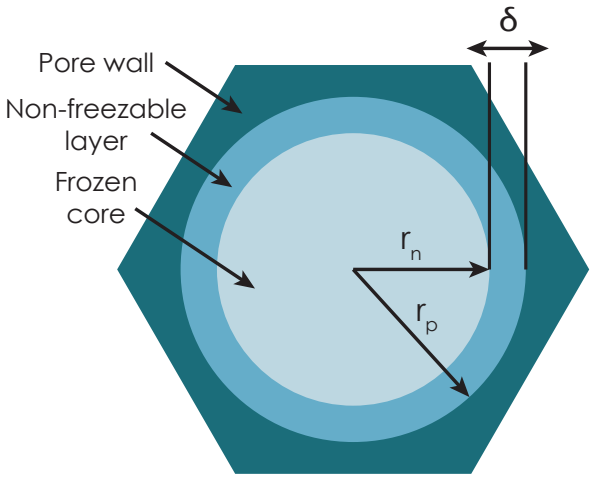

Figure S21: Schematic representation of probe confined within a pore - while core is solidified, strongly adsorbed solvent remains in contact with the pore wall as a non-freezable layer of thickness δ.

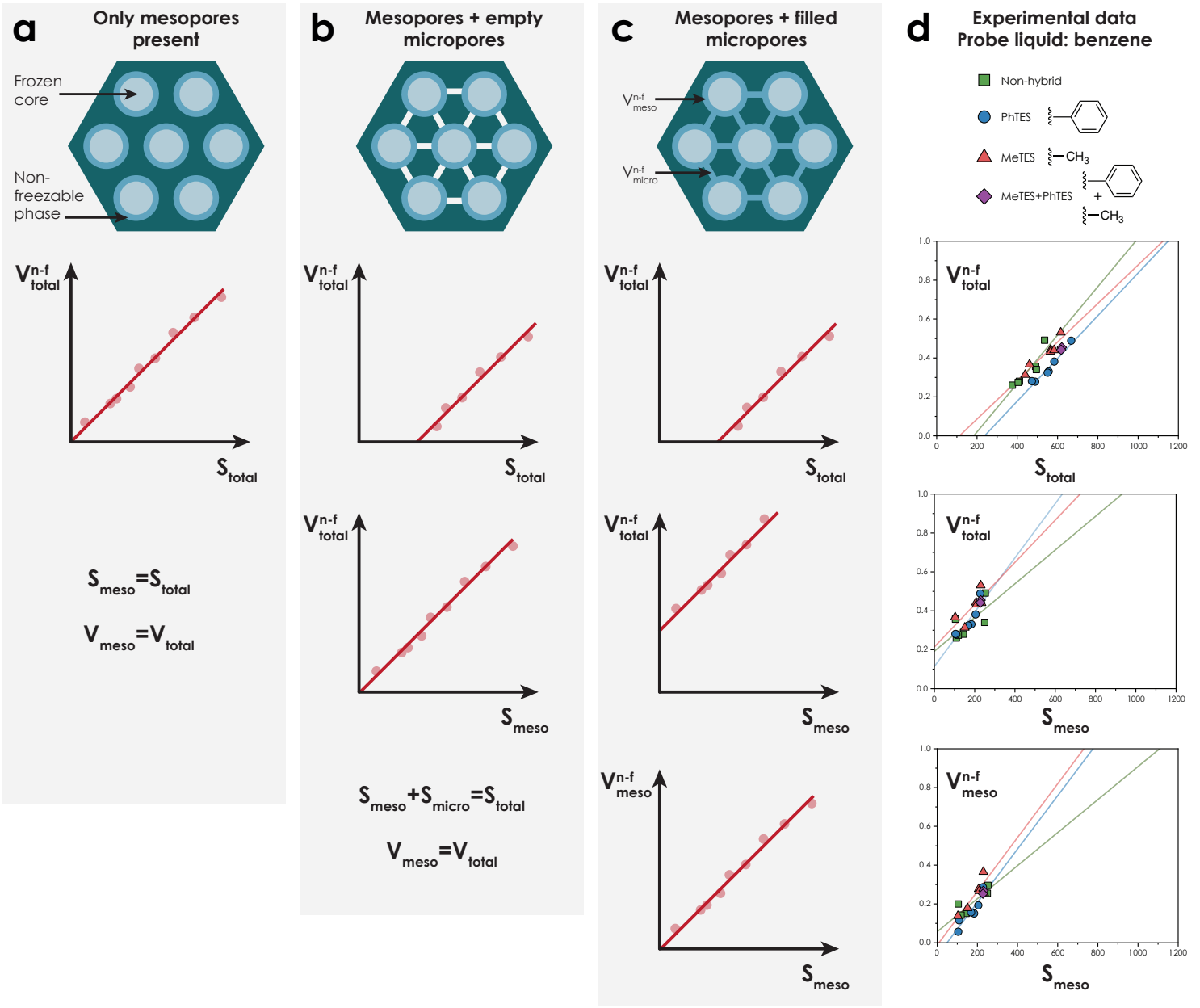

Figure S22: Scheme illustrating how the relation between non-freezable volume V^{n-f} evolves as a function of surface area S depending on the degree of filling the micropores: (a) In a non-microporous material V^{n-f} arises only from a non-freezable layer of thickness δ adjacent to the mesopore wall; (b) If micropores are present but they are not penetrated by solvent, they contribute to S value, but not to V^{n-f} - to obtain $V^{n-f} = f(S)$ with zero intercept, the S_{micro} must be substracted from S_{total}; (c) for filled micropores real V^{n-f} is lower than expected due to high pore curvature and the $\delta > r_{micro}$ relation.

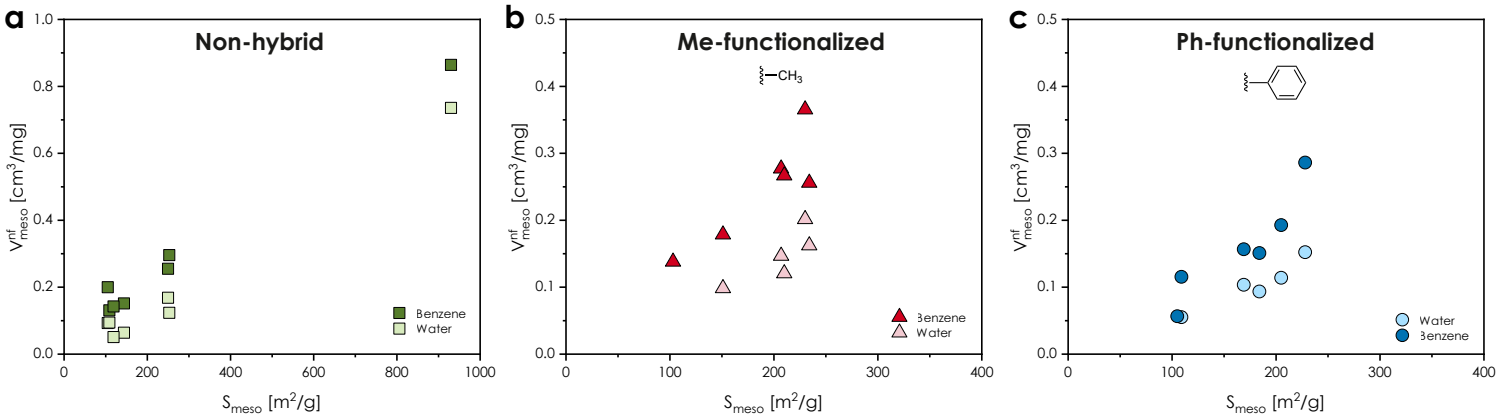

Figure S23: Volume of non-freezable water (brighter colors) and benzene (darker colors) as a function of the specific surface area for (a) non-hybrid samples; (b) Me-functionalized samples; (c) Ph-functionalized samples.

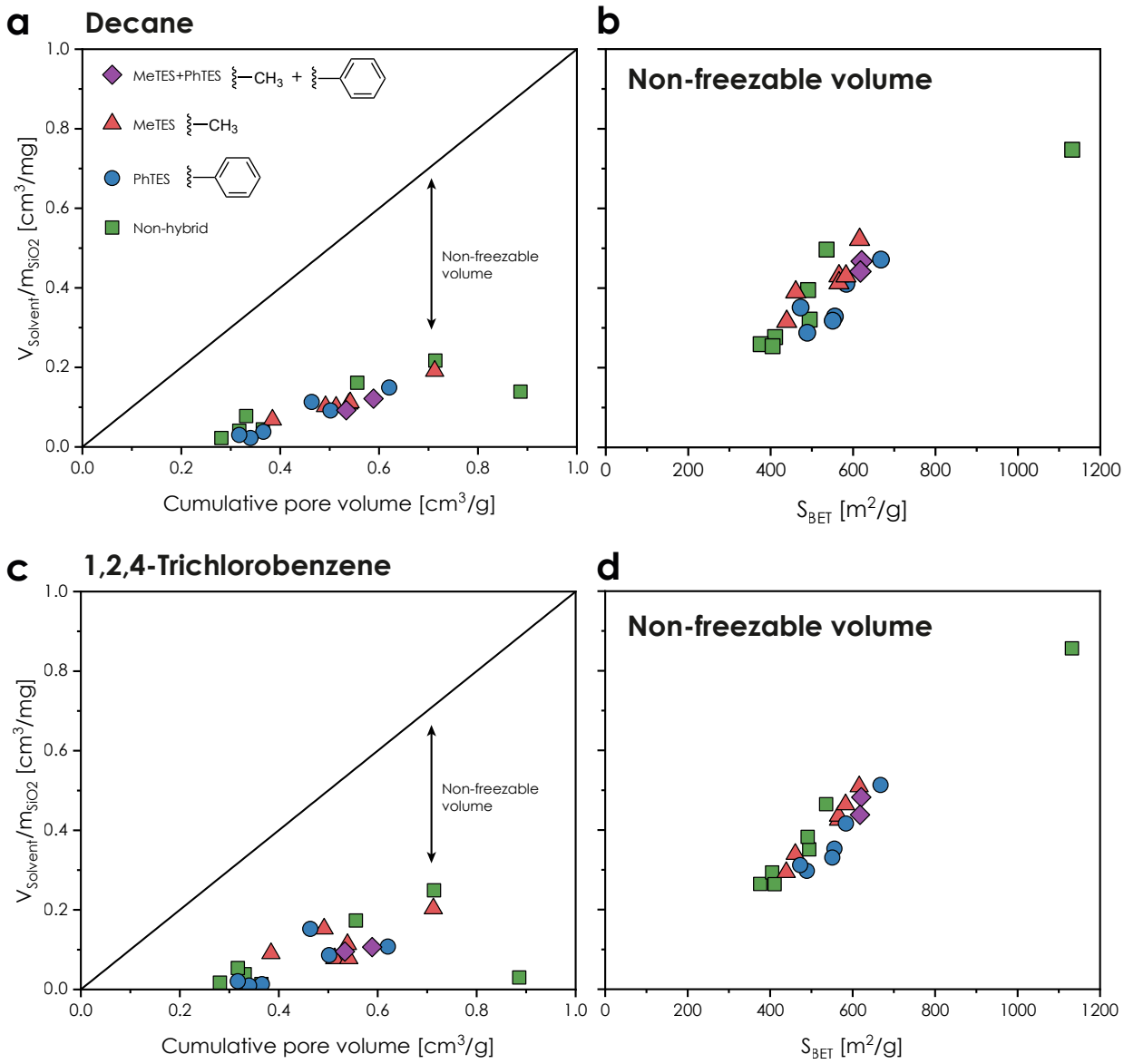

Figure S24: Volume of solvent undergoing the melting transition in pores (as a function of cumulative pore volume measured by N_2 sorption) and volume of non-freezable solvent (as a function of the specific surface area) obtained for decane (a), (b) and for TCB (c), (d). Green squares correspond to non-hybrid samples. Red, blue, and purple points represent powders functionalized with Me, Ph, and Me+Ph groups, respectively.

References

(1) Landry, M. R. Thermoporometry by differential scanning calorimetry: experimental considerations and applications. *Thermochim. Acta* **2005**, *433*, 27–50.

(2) Tonutti, L. G.; Maquirriain, M. A.; Querini, C. A.; Dalla Costa, B. O. Synthesis of sulfonic SBA-15 by co-condensation and soxhlet extraction: optimization by shortening the preparation time. *J. Porous Mater.* **2022**, *30*, 33–42.

(3) Su, Y. L.; Wang, J.; Liu, H. Z. Melt, hydration, and micellization of the PEO-PPO-PEO block copolymer studied by FTIR spectroscopy. *J. Colloid Interface Sci.* **2002**, *251*, 417–423.

(4) Su, Y.-l.; Wang, J.; Liu, H.-z. FTIR Spectroscopic Study on Effects of Temperature and Polymer Composition on the Structural Properties of PEO-PPO-PEO Block Copolymer Micelles. *Langmuir* **2002**, *18*, 5370–5374.

(5) Riikonen, J.; Salonen, J.; Lehto, V.-P. Utilising thermoporometry to obtain new insights into nanostructured materials. *J. Therm. Anal. Calorim.* **2010**, *105*, 811–821.

(6) Majda, D.; Zimowska, M.; Tarach, K.; Góra-Marek, K.; Napruszewska, B. D.; Michalik-Zym, A. Water thermoporosimetry as a tool of characterization of the textural parameters of mesoporous materials. *J. Therm. Anal. Calorim.* **2016**, *127*, 207–220.

(7) Ishikiriyama, K.; Todoki, M. Pore Size Distribution Measurements of Silica Gels by Means of Differential Scanning Calorimetry. *J. Colloid Interface Sci.* **1995**, *171*, 103–111.

(8) Bahloul, N.; Baba, M.; Nedelec, J. M. Universal behavior of linear alkanes in a confined medium: toward a calibrationless use of thermoporometry. *J. Phys. Chem. B* **2005**, *109*, 16227–16229.

(9) Brun, M.; Lallemand, A.; Quinson, J.-F.; Eyraud, C. A new method for the simultaneous determination of the size and shape of pores: the thermoporometry. *Thermochim. Acta* **1977**, *21*, 59–88.

(10) Billamboz, N.; Baba, M.; Grivet, M.; Nedelec, J.-M. A General Law for Predictive Use

of Thermoporosimetry as a Tool for the Determination of Textural Properties of Divided Media. *J. Phys. Chem. B* **2004**, *108*, 12032–12037.

(11) Prouzet, E.; Cot, F.; Nabias, G.; Larbot, A.; Kooyman, P.; Pinnavaia, T. J. Assembly of mesoporous silica molecular sieves based on nonionic ethoxylated sorbitan esters as structure directors. *Chemistry of materials* **1999**, *11*, 1498–1503.